Ultrafast real-time observation of double Fano resonances in discrete excitons and single plasmon-continuum

R. K. Chowdhury,[1] S. Mukherjee,[1] S. N. B. Bhaktha,[1] and S. K. Ray[1,2]
[1]*Department of Physics, Indian Institute of Technology Kharagpur, Kharagpur 721302, India*
[2]*S. N. Bose National Centre for Basic Sciences, Kolkata 700106, India*

(Received 14 November 2019; revised manuscript received 3 June 2020; accepted 9 June 2020; published 29 June 2020)

Ultrafast observation of multiple asymmetric Fano line shapes in energetically overlapped single continuum and multiple discrete states is of great theoretical interest in different domains of physics, though their real-time experimental demonstrations are yet to be achieved. Here, we present an experimental observation on time-domain response of the double Fano asymmetries in a metal–two-dimensional semiconductor hybrid prototype at room temperature. The ultrafast interactions in two discrete spin-resolved excitons of MoS_2 and a single metal plasmon-continuum allow us to observe the generation and evolution of the double Fano line profiles in real time. Apart from the subpicosecond development of double Fano line shapes, we calculate all the time-dependent nonlinear double Fano parameters. These results suggest a better understanding of ultrafast Fano physics in condensed-matter systems and have potential prospects in ultrafast photonic devices using double Fano resonances even at room temperature.

DOI: 10.1103/PhysRevB.101.245442

I. INTRODUCTION

The Fano resonance, a quantum mechanical interference phenomenon, observed when one or many discrete states are energetically overlapped with a continuum, commonly occurs in different branches of physics starting from atomic to condensed-matter domains [1–4]. Typically Fano resonances are identified by their asymmetric line shapes, which arise due to the constructive and destructive interference around the resonant energy of the discrete state. This unusual phenomenon was first addressed by U. Fano in his theoretical work on the autoionization process of the He atom [5], although its ultrafast temporal evolution has been experimentally demonstrated recently via extreme-ultraviolet pump-probe spectroscopy [6,7], whereas the line shapes can be further probed using a second pulse after the primary pump excitation that is beyond the perturbation limit of the pump [8–10]. On the contrary, in condensed-matter systems, several theoretical studies have been reported on ultrafast growth and time reversal of nonlinear Fano resonances in metal-semiconductor hybrid systems on femtosecond timescales [11–14]. Although a few experimental observations on coherent phonon-mediated temporal evolution of a single Fano line shape have been reported in bulk semiconductors (GaAs, Si, Ge, etc.) under extreme experimental conditions such as ultralow temperature and high magnetic fields [15–18], the room-temperature time-resolved evolution of double Fano resonances in condensed-matter systems is still unexplored.

Interestingly, two-dimensional (2D) layered semiconductors such as transition-metal dichalcogenides (TMDs) offer a unique platform, where two discrete excitonic states can coexist simultaneously due to their strong spin-orbit coupled band splitting [19,20]. In layered TMDs like MoS_2, the splitting is as high as ∼150 meV due to the reduced dielectric screening and modified Coulomb interactions in a 2D stratum [21]. Strong light-matter interactions thus result in the formation of two energetically well-separated spin-resolved excitons, X_A^0 at ∼1.8 eV (675 nm) and X_B^0 at ∼2.0 eV (615 nm), with a typical exciton binding energy greater than the thermal energy at room temperature [22]. The Purcell enhancement and polaritonic properties of these excitons were demonstrated previously in MoS_2 in weak and strong near-field coupling regimes, respectively [23,24]. On the other hand, it is known that metal nanostructures can act as a continuum of plasmonic hot spots depending on their size distributions and interspacing distances. Therefore, the strong coupling between these discrete excitons and a plasmon-continuum in properly designed metal-TMD hybrid nanostructures can satisfy the requirements of the Fano resonance [25–27]. In fact, these two excitons (X_A^0 and X_B^0) with high excitonic binding energy in TMDs can provide a pathway to achieve two distinguishable asymmetrical Fano features in the same spectrum at room temperature, if one can tailor the plasmon-continuum to accomplish successful overlap with both of the discrete excitonic states.

In this report, we experimentally demonstrate the time-resolved evolution of novel double Fano line shapes in a precisely designed exciton (MoS_2)–plasmon (Au) hybrid in a condensed-matter system via femtosecond transient spectroscopy at room temperature. The self-assembled Au nanodisks, created by dewetting, serve as the continuum of surface plasmons, whereas the MoS_2 acts as the source of paired discrete states in terms of two spin-resolved excitons (X_A^0 and X_B^0). The resonant coupling regime for both the excitons and plasmons is demonstrated within the 600–700 nm spectral range, as shown in the measured and simulated steady-state

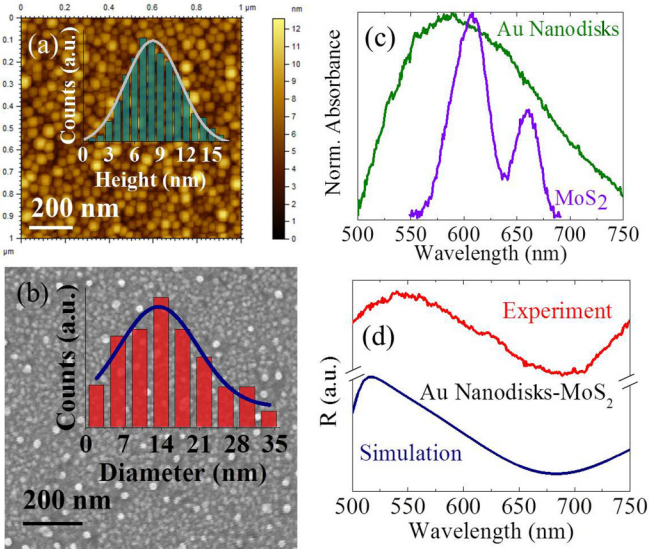

FIG. 1. Structural and optical characterizations for Au-MoS_2 hybrids. (a) Typical AFM image of Au nanoislands and the corresponding histogram (inset) showing the height distribution with an average value ∼7.0 nm. (b) Typical FESEM micrograph and corresponding inset show the lateral size distribution of Au nanoislands revealing the formation of Au nanodisks on top of MoS_2. The average diameter of the Au nanoislands is ∼14.0 nm. (c) Steady-state normalized absorption spectra of Au nanodisks and MoS_2 layers. (d) Experimentally measured and simulated steady-state reflectivity (R) spectra of Au-MoS_2 hybrid along with substrate.

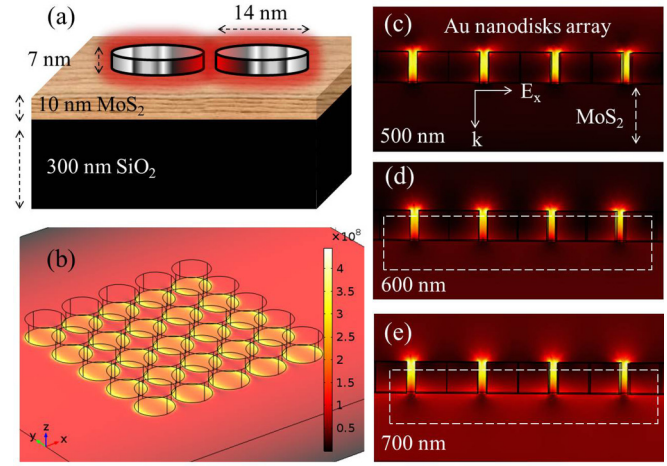

FIG. 2. E-field distribution for Au-MoS_2 hybrid structure. (a) The schematic representation of Au nanodisks on layered MoS_2. (b) In-plane electric-field coupling (675 nm) at the interface of Au nanodisks and MoS_2. Panels (c), (d), and (e) show the out-of-plane E-field distribution at off-resonant and resonant conditions (rectangle with white-colored dashed line) suggesting that the metal (Au)–semiconductor (MoS_2) coupling is activated near the excitonic absorption (within 600–700 nm) of MoS_2. The input wave is propagating along the k direction.

reflectivity profile. While monitoring in the time domain, a typical double Fano line shape formation is observed at ∼1.0 ps delay. Furthermore, we show that double Fano asymmetries and their corresponding Fano parameters (q_{ex} and Γ_{ex}) are persistent up to 5.0 ns, the upper limit of the instrumental time delay in our setup. Our results thus demonstrate the subpicosecond growth of a unique double Fano resonance phenomenon in metal–2D semiconductor hybrid systems, which may pave the way for real-time control over ultrasensitive photoresponse in photonic devices via tailoring their exciton-plasmon coupling.

The rest of the paper is organized as follows. In Sec. II, we present experimental observations along with theoretical investigations. First, we explain the formation of double Fano resonances in the Au-MoS_2 hybrid in detail. Then, we discuss the time evolution of the double Fano line shapes along with their nonlinear modulations. Finally, in Sec. III, we give a brief summary and outlook.

II. RESULTS AND DISCUSSION

Wafer-scaled MoS_2 was grown using chemical vapor deposition on top of a 300 nm thick SiO_2/Si wafer. Thereafter, self-assembled Au nanoislands were fabricated on top of the MoS_2 layers through the rapid thermal dewetting of as-deposited ultrathin gold film under high vacuum (details in Appendix A). The height profile of a typical atomic force micrograph (AFM) analysis [Fig. 1(a) and corresponding inset] reveals the average height of the Au nanoislands to be around ∼7.0 nm. On the other hand, field-emission scanning electron micrographs (FESEMs) and corresponding histograms confirm an average diameter of Au nanoislands to be ∼14.0 nm [Fig. 1(b) and corresponding inset] which supports the formation of Au nanodisks on top of MoS_2. Prior to the recording of transient spectra, we measured the steady-state absorption and reflection profiles of our samples. Comparative steady-state absorption spectra of Au nanodisks and layered MoS_2 are shown in Fig. 1(c), which ensures that both of the excitonic peaks overlap with the broad plasmon-continuum, an essential criterion to accomplish double Fano resonances. It is to be noted that we are unable to observe Fano characteristics in the steady-state measurements for the Au-MoS_2 hybrid system, as the power density (∼0.1 W/cm^2) of our available far-field UV-visible spectroscopy setup is inadequate to achieve the Fano interference criterion [12,13]. The steady-state reflectivity spectrum of the fabricated Au-MoS_2 hybrids is shown in Fig. 1(d). Interestingly, the experimental reflectivity spectrum is in close agreement with the simulated (COMSOL Multiphysics) results, though the disagreement at a lower wavelength is possibly due to the inevitable size distribution of self-assembled Au nanoislands [see the histograms in the insets of Figs. 1(a) and 1(b)], which was not considered in our simulation (Appendix B). The simulated prototype structure consists of Au nanodisks 7.0 nm in height and 14.0 nm in diameter, on top of the 10.0 nm thick MoS_2 over a 300 nm thick SiO_2/Si, as shown in Fig. 2(a). A typical in-plane electric field (E_X) distribution [Fig. 2(b)] along the interface of the Au nanodisk array (5×5) and MoS_2 confirms the formation of Au hot spots on top of MoS_2, as light usually traps more efficiently at the metal-semiconductor interface. Furthermore, a strong resonant out-of-plane coupling is observed at the interface of Au nanoislands and MoS_2 in the wavelength range 600–700 nm, which disappeared at 500 nm [Figs. 2(c)–2(e)].

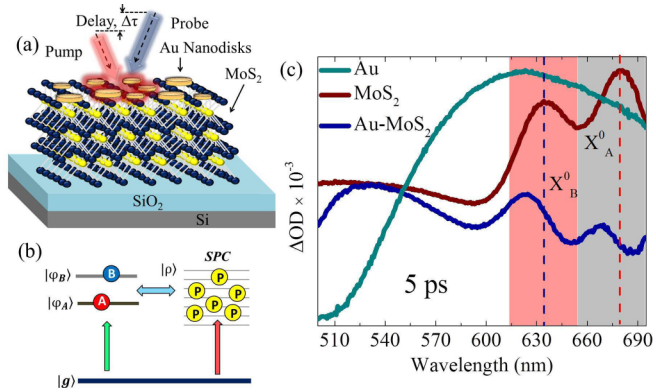

FIG. 3. Real-time mapping of double Fano resonances: scheme and results. (a) Schematic of the sample structure for noncollinear pump-probe measurements to investigate the evolution of double Fano line shapes in the time domain (i.e., as a function of time delay, $\Delta\tau$) using self-assembled Au nanodisks/layered MoS_2 system. (b) A graphical representation of the Fano interference scheme between double discrete spin-orbit (SO) coupled excitons (X_A^0 and X_B^0) of MoS_2 and a single plasmon-continuum (P) due to self-assembled Au nanodisks. (c) Transient spectra for Au nanostructures, pristine MoS_2, and Au-MoS_2 hybrid at 5.0 ps probe delay for 1.0 GW/cm^2 pump power, depicting clear double Fano line shape for both of the exciton-plasmon overlaps for Au-MoS_2 hybrid (blue curve).

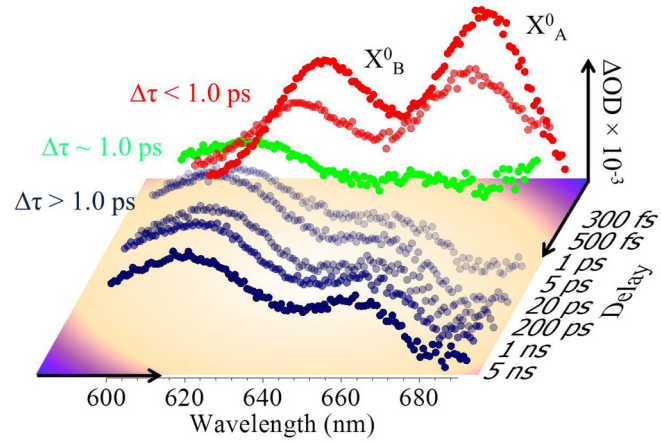

FIG. 4. Typical ultrafast transient spectra (pump power density, $P_{pump} \sim 10^9$ W/cm^2) of Au-MoS_2 hybrid nanostructures in 600–700 nm wavelength range. The ΔOD spectra with red points at 300 and 500 fs probe delay represent the excitonic peaks (X_A^0 and X_B^0) of MoS_2 within the first 500 fs, suggesting that discrete excitons and continuum of plasmons are not coupled together. On the contrary, the curve with green points is at an intermediate-coupling limit for 1.0 ps probe delay. Thereafter, the coupling between excitons and plasmons becomes robust displaying Fano line shapes up to a delay of 5.0 ns.

In our study, we have chosen a few-layer MoS_2 instead of a monolayer to enhance the out-of-plane dipolar coupling between Au and MoS_2 by confining the plasmon-enhanced E field in the semiconductor, as suggested in the earlier report [28].

In an earlier work on metal–2D TMD hybrids, Lee *et al.* [25] demonstrated the possibility to achieve double Fano line shapes via steady-state reflectivity ($\Delta R/R$) measurements at low temperature, though their Fano features mainly appeared at the spectral range of X_A^0. However, herein for our 2D TMD–plasmonic system, the Fano line shapes originate from the coherent Coulomb interactions and strong many-body effect in the presence of high pump power density ($P_{pump} \sim$ GW/cm^2) and can be considered as nonlinear Fano effects because of their excitation power dependency [12,13], unlike from the conventional Fano resonance for atoms. In our case [Fig. 3(a)], the nonresonant pumping (430 nm, 1.0 GW/cm^2) initiates the dynamic growth of the Fano resonances by induced dipole moments of oscillating spin-orbit (SO) coupled discrete excitons (X_A^0 and X_B^0) in MoS_2 and also produces the coherently coupled surface plasmon continuum (SPC). Following this, the time-delayed broadband probe pulse (400–700 nm) is then used to capture the exciton-plasmon interactions within the radiative decay time limit of excitons in few-layer MoS_2 (details in Appendix C). A typical twofold Fano interference scheme is shown in Fig. 3(b) consisting of two discrete SO-coupled excitons (X_A^0 and X_B^0) that energetically overlap with the SPC. Comparative transient spectra of the Au nanostructure, pristine MoS_2, and the Au-MoS_2 hybrid show the ultrafast formation of the double Fano line shapes in the case of the hybrid, as shown in Fig. 3(c). The broad size distribution of Au nanoislands is the reason behind the formation of a broad plasmon-continuum, which is essential to realize the Fano line shapes.

Experimentally measured transient spectra in Fig. 4 show the ultrafast formation of the double Fano line shapes in the time domain. For the positive probe delays ($\Delta\tau$), the broadband probe (400–700 nm) arrives after the pump excitation. In the beginning ($\Delta\tau < 1$ ps), the coupling between the excitons and the plasmon-continuum is vague. Transient spectra (red points, Fig. 4) clearly display two discrete excitonic peaks (X_A^0 and X_B^0) of MoS_2 at 300 and 500 fs, which are weakly coupled with the continuum in this particular time domain. This possibly happens because of the activation of the ultrafast strong Auger scattering process in the excitons, which typically occurs on a similar timescale. This process would later result in the formation of the stable hot-exciton population in the 2D MoS_2 stratum on a relatively higher timescale (~ps). At $\Delta\tau \sim 1.0$ ps (green points, Fig. 4), the effect of exciton-plasmon coupling is moderate, and the spectral asymmetrical line shape is developing. Afterward, for $\Delta\tau > 1.0$ ps (blue points, Fig. 4), the strong exciton-plasmon coupling brings the system into the Fano resonance limit. In this time domain ($\Delta\tau > 1.0$ ps), both the excited excitonic and plasmonic states are stable. The interference among these states thus grows with time. The energetically overlapped oscillating dipoles have acquired enough time to produce strong optical signals. This contributes to narrower spectral line shapes at higher delay ($\Delta\tau$) as shown in the normalized transient optical density (ΔOD) spectra (Fig. S5 of the Supplemental Material [29]). We have also calculated the momentary reflectivity $R(t)$ for two different probe delays that further confirms the incremental asymmetrical nature of double Fano resonances at higher delay (Fig. S6 of the Supplemental Material [29]). It is important to note that the instrumental delay limit of our present experimental setup is 5.0 ns. Interestingly, the

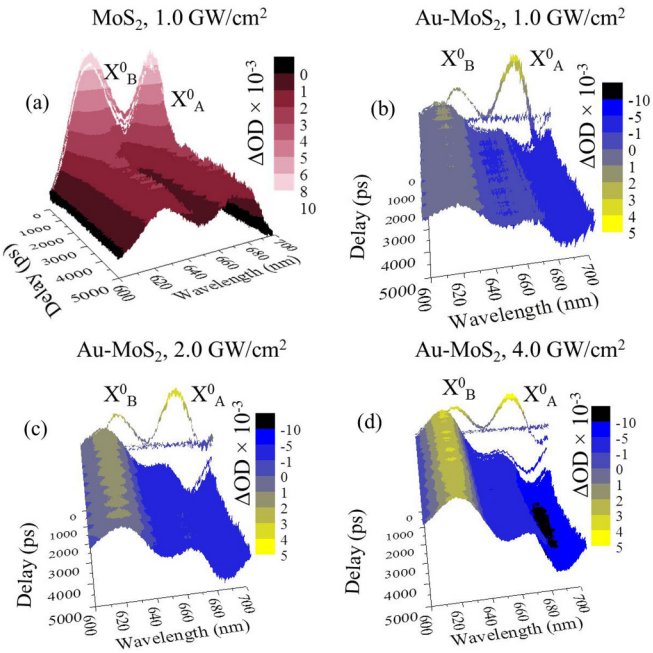

FIG. 5. Nonlinear response of double Fano resonances. (a) Transient spectra of as-grown pristine MoS_2 on 300 nm SiO_2 substrates revealing both of the discrete excitonic peaks (X^0_A and X^0_B). Panels (b)–(d) display the pump-power-dependent (1.0, 2.0, and 4.0 GW/cm^2) ultrafast observation of asymmetrical line shapes as a result of coupling between discrete spin-resolved excitons from TMDs and continuum of plasmons from metal nanostructures. The power-dependent transient mapping supports the evolution of nonlinear Fano resonance in Au-MoS_2 hybrid systems.

double Fano profiles become sharpest on the timescale of the nonradiative lifetime of excitons in MoS_2 ($\Delta\tau \sim 20.0$ ps). On the other hand, at higher probe delays ($\Delta\tau \sim$ ns), double Fano asymmetries are dominated via thermalization or carrier cooling of pump-induced hot excitons from the surface to inner layers of few-layered MoS_2 via incoherent phonon exchange [28], which extends the exciton-plasmon coupling timescale beyond the excitonic radiative time limit of conventional monolayer MoS_2.

In order to support the premise of the nonlinear contribution of the Fano resonance in our Au-MoS_2 hybrid system, we increased pump power gradually by keeping other experimental conditions unaltered. In principle, there is no difference in terms of spectral asymmetries and physical origin between the conventional and nonlinear case. The only variation is the dependence and evolution of the Fano line shapes with the incident pump power [12,13], which we are going to discuss next. As a control sample, we first measured the transient spectra (430 nm, 1.0 GW/cm^2 pump) of the as-grown pristine MoS_2 layers without any Au nanodisks on top [Fig. 5(a)]. The spectral positions of both of the spin-orbit coupled excitons (X^0_A and X^0_B) of MoS_2 are revealed. It is important to mention here that we have considered mutually noninteracting excitons in MoS_2, since the typical line spacing between X^0_A and X^0_B is calculated to be ∼150 meV. So, both of the excitons are presumed to interact individually with the continuum (SPC) of Au plasmons resulting in the double Fano resonances profile in real time. In the case of a condensed-matter system, it is very pertinent to observe pump-intensity-dependent evolution of Fano line shapes, as predicted by various earlier theoretical reports [12,13]. Following that, we have observed the double Fano line shape generation for a fixed temporal domain ($\Delta\tau = -5.0$ ps to $\Delta\tau = 5.0$ ns) at different pump power densities ($P_{\text{pump}} = 1.0$, 2.0, and 4.0 GW/cm^2) within the damage threshold limit for our fabricated prototype, as shown in Figs. 5(b)–5(d). It is evident from the color contrast of the ΔOD spectra ($\Delta\tau > 1.0$ ps) that line profiles of both of the double Fano resonances gradually increase with the increase in pump power density. The modification of the double Fano line shapes with increasing pump power indeed confirms the nonlinear evolution of the Fano spectra for our fabricated Au-MoS_2 hybrid.

We next calculated the time-resolved nonlinear Fano parameters (q_{ex} and Γ_{ex}) for both of the excitons (X^0_A and X^0_B) at 5.0 ps and 5.0 ns time delay ($\Delta\tau$). The transient optical density (ΔOD) is given by (detailed calculations in Appendix D)

$$\Delta\text{OD}|_{\Delta\tau} \propto \text{Re}\left\{\left[1+\frac{(q_A-i)^2}{1-i\epsilon_A}\left(1-e^{-\frac{\Gamma_A}{2}(1-i\epsilon_A)\Delta\tau}\right)\right] \times\left[1+\frac{(q_B-i)^2}{1-i\epsilon_B}\left(1-e^{-\frac{\Gamma_B}{2}(1-i\epsilon_B)\Delta\tau}\right)\right]\right\}, \quad (1)$$

where $\epsilon_{ex}|_{(ex=A\,or\,B)} = \frac{2(E-E_{ex})}{\Gamma_{ex}}$, q_{ex} = the Fano asymmetry parameter, Γ_{ex} = Fano linewidth, and E_{ex} = energy of discrete state (here, exciton). It is important to note that the temporal limit of our instrumental response time is $\Delta\tau \sim$ 250 fs. The experimental data could only be recorded beyond this threshold time limit. The experimental studies confirm that the strong coupling between excitons and plasmons is achieved within 1.0–5.0 ps. At higher pump power density ($P_{\text{pump}} \geqslant 1.0$ GW/cm^2), the strong many-body effect and modified Coulomb interactions in excitons may be playing a critical role, which shows the weak coupling of excitons and plasmon at lower probe delay ($\Delta\tau < 1.0$ ps) until the system reaches the strong-coupling limit temporally ($\Delta\tau >$ 1.0 ps). We thus only focus on the line shapes of the double Fano profile in the picosecond time domain and onward to calculate the Fano parameters (q_{ex} and Γ_{ex}), as tabulated in Table I. The nonlinear Fano asymmetry parameters (q_{ex}) show a value of ∼1.5 and 2.0 for the respective exciton (X^0_A and X^0_B)–plasmon (P) coupling, whereas the FWHM (Γ_{ex}) value is ∼80 meV for both the cases on average. These parameters (q_{ex} and Γ_{ex}) for both of the coupled exciton-plasmon appear to be delay ($\Delta\tau$) independent, as we move more toward the nonlinear regime ($P_{\text{pump}} \sim 4.0$ GW/cm^2). The Fano resonance mechanism in the coupled exciton-plasmon system is primarily controlled by two processes [30]: (i) coherent dipole exchange of X^0 and P, and (ii) incoherent photon exchange between one emitter along with subsequent reabsorption by another. The first process occurs rapidly within a few tens of fs (∼50 fs) that can be associated with the Γ_{ex} (80 meV) of the double Fano line shape, which is beyond our experimental delay limit. On the other hand, the second process leads to the formation of relatively stable Fano profiles on higher timescales (∼ps). It may be imperative to mention here that a

TABLE I. Nonlinear Fano parameters (q_{ex} and Γ_{ex}), as calculated from pump power density (P_{pump}) dependent transient measurements.

Exciton-plasmon (X^0-P)	Probedelay ($\Delta\tau$)	P_{pump} (GW/cm^2) 1.0 q_{ex}	1.0 Γ_{ex}	2.0 q_{ex}	2.0 Γ_{ex}	4.0 q_{ex}	4.0 Γ_{ex}
X_A^0-P	5.0 ps	0.9 ± 0.05	69 ± 13	1.2 ± 0.02	69 ± 22	1.3 ± 0.10	77 ± 2
	5.0 ns	1.2 ± 0.06	69 ± 9	1.4 ± 0.03	72 ± 7	1.6 ± 0.03	63 ± 18
X_B^0-P	5.0 ps	1.3 ± 0.02	140 ± 36	2.0 ± 0.07	80 ± 5	2.0 ± 0.08	80 ± 9
	5.0 ns	1.5 ± 0.03	92 ± 20	1.7 ± 0.01	69 ± 13	1.9 ± 0.02	75 ± 4

rigorous time-domain calculation [31] considering the many-body interactions in nonresonant background, multiexcitonic processes and nonlinear responses are required, which is still an open problem to explore. In any case, the present results ubiquitously reveal the transient evolution of double Fano resonances in a plasmonic–2D materials hybrid system and achieve a significant landmark in the field.

III. CONCLUSIONS

In summary, our femtosecond transient measurements reveal the real-time observation of double Fano resonance profiles at room temperature in a condensed-matter system (Au-MoS_2 hybrid), as theoretically predicted earlier [5,12]. Two-dimensional MoS_2 plays a vital role here having two energetically well separated strongly bound discrete excitons (X_A^0 and X_B^0), both spectrally (600–700 nm) and temporally correlated with the single metal plasmon-continuum, leading to the formation of double Fano line shapes in the time domain. The ultrafast evolution of the double Fano resonance starts on a timescale of $\Delta\tau > 1.0$ ps and was found to be sustained even at 5.0 ns, the upper time limit of our instrumental delay. Moreover, the nonlinear transient modulations of the double Fano resonances are established through measurements with variable pump power density ($P_{\text{pump}} \sim 1.0$ to 4.0 GW/cm^2). Extracted nonlinear Fano parameters (q_{ex} and Γ_{ex}) are found to be ∼1.5 and ∼80 meV for both of the Fano line shapes (X_A^0-P and X_B^0-P). Our study on time-resolved double Fano resonances thus provides imperative evidence of strongly coupled exciton-plasmon dynamics in metal–2D semiconductor hybrid platforms, which may offer new prospects in ultrafast two-level all-optical sensors and switches [1,32–34].

ACKNOWLEDGMENTS

We acknowledge the SDGRI-UPM project of IIT Kharagpur for necessary equipment support at the Ultrafast Science Lab, Department of Physics, IIT Kharagpur.

APPENDIX A: SAMPLE FABRICATION AND CHARACTERIZATION

Wafer-scale few-layered MoS_2 (∼10.0 nm) film was grown uniformly on SiO_2 (∼285 nm)/Si substrates by the chemical vapor deposition technique. At first, a very thin Mo film of ∼5.0 nm thickness was deposited directly on the substrates by electron-beam evaporation (chamber pressure $\sim 2 \times 10^{-6}$ mbar) and subsequent sulfurization at an optimum temperature (680 °C) under the control atmosphere (H_2:Ar ∼ 1:4) resulting in the formation of ∼10 nm thick MoS_2 film. Thereafter, an ultrathin Au film (∼5.0 nm) was deposited on top of the MoS_2 surface via thermal evaporation technique. The required self-assembly of Au nanostructures was obtained directly through dewetting of the as-deposited Au film at a constant annealing temperature of 250 °C for 3 hours in a vacuum ($\sim 10^{-6}$ mbar), resulting in the formation of Au nanodisks with an average height of ∼7.0 nm and average diameter of ∼14.0 nm. The lateral size distribution of Au nanostructures was examined via a ZEISS SUPRA-40 field-emission scanning electron microscope (FESEM). The height profile was analyzed using an Agilent Technology 5500 atomic force microscope (AFM). The chemical composition and pristine materialization of our fabricated samples are analyzed by the ULVAC-PHI, Inc., Auger electron spectroscopy and PHI 5000 VersaProbe II, ULVAC-PHI, Inc., x-ray photoelectron spectroscopy with incident Al K_α x rays.

APPENDIX B: NUMERICAL SIMULATION

The steady-state reflectivity of our fabricated system was simulated by a numerical model based on Fresnel's equation using the RF module of the COMSOL Multiphysics (5.1) software. The structure of the sample was optimized by simulating the effect of the dimension and geometry of Au nanostructures as well as the thickness of MoS_2 layers on the E-field distribution and resultant reflectivity spectrum (Fig. 2, and Fig. S3 of the Supplemental Material [29]). An optimized thickness (∼10.0 nm) of MoS_2 on top of 300 nm SiO_2 substrate was chosen for the simulation. Initially, the shape of Au nanostructures was varied from hemispherical to disklike, matching the average dimension (14.0 nm diameter, 7.0 nm height) of the experimentally fabricated Au-MoS_2 system. The thickness of the MoS_2 layers was also varied from 1.0 nm to 10.0 nm by keeping the dimension of the nanodisks unaltered, to achieve efficient E-field coupling, which was found higher with increasing number of layers, as reported earlier. The wavelength-dependent refractive index of each medium (SiO_2, MoS_2, Au, and air) was chosen from the available COMSOL library, which is essential for solving Fresnel's equations.

APPENDIX C: DETAILS OF STEADY-STATE AND TRANSIENT MEASUREMENTS

Steady-state reflectivity measurements were performed using a PerkinElmer spectrometer within a wavelength range of 300–800 nm. A Newport transient spectrometer equipped with a Si-photodiode array was used to measure the time-

resolved differential signal ($\Delta\text{OD} = \text{OD}_{\text{pump-on}} - \text{OD}_{\text{pump-off}}$) spectra using a Ti:sapphire laser (808 nm, 50 fs, 2.9 W) with 1 kHz repetition rate. Now, depending on the transparency of the sample, we used the reflection or transmission geometry of the setup by controlling the in-built phase tool in our commercially available TAS software (Newport). The pump beam (430 nm, ∼2.0 mm spot size) was generated via optical parametric amplification technique (TOPAS-Prime, Coherent) from the major part of the laser beam, while the remaining part was focused on a CaF_2 crystal, generating a continuum probe (400–700 nm, ∼0.15 mm spot size) to result in a noncollinear pump-probe setup. The probe path was attached with a motorized transnational stage (Newport) to introduce varying time delays. The transient spectra were recorded by chopping the pump beam at 500 Hz to achieve consecutive on and off probe spectra for each laser pulse.

APPENDIX D: ANALYTICAL THEORY FOR DOUBLE FANO RESONANCES

The time-dependent wave functions and corresponding coefficients for the exciton-plasmon overlap have been solved analytically using time-dependent Schrödinger equations by following several earlier theoretical reports [5,6,35].

The energy matrix elements for the double Fano profile are [5]

$$\langle\phi_A|H|\phi_B\rangle = E_A\delta_{AB}, \tag{D1}$$

$$\langle\rho|H|\phi_{A\,or\,B}\rangle = V_{A\,or\,B}, \tag{D2}$$

$$\langle\rho'|H|\rho\rangle = E\delta(E'-E). \tag{D3}$$

Here, $|\phi_A\rangle$ and $|\phi_B\rangle$ denote the mutually orthogonal wave functions of the excitonic states of A and B excitons, respectively, whereas $|\rho\rangle$ denotes the plasmon-continuum. We have considered mutual noninteractions between both of the spin-orbit coupled excitons (X_A^0 and X_B^0), $\delta_{AB} = 1$, for $A = B$ in Eq. (D1).

Now, following the theoretical method undertaken earlier [6,35], the time-dependent transition dipole moments [$T_A(t)$ and $T_B(t)$] for both of the exciton (X_A^0 and X_B^0)–plasmon (P) interactions are

$$T_A(t) \sim i\left[2\delta(t) + \frac{\Gamma_A}{2}(q_A - i)^2 e^{-i\epsilon_A t} e^{-\frac{\Gamma_A}{2}t}\right], \tag{D4}$$

$$T_B(t) \sim i\left[2\delta(t) + \frac{\Gamma_B}{2}(q_B - i)^2 e^{-i\epsilon_B t} e^{-\frac{\Gamma_B}{2}t}\right], \tag{D5}$$

where $\Gamma_A = 2\pi {V_A}^2$ and $\Gamma_B = 2\pi {V_B}^2$ are the width of resonance for the exciton-plasmon interactions, q_A and q_B are the double Fano asymmetry parameters, and $\epsilon_A = \frac{2(E-E_A)}{\Gamma_A}$ and $\epsilon_B = \frac{2(E-E_B)}{\Gamma_B}$ are the rescaled energy.

To transfer these elements in the energy domain, we have to perform the Fourier transform of these transition dipole moments for the finite $\Delta\tau$ probe delay. Therefore, the change in optical density (ΔOD) for both of the exciton-plasmon interactions (X_A^0-P and X_B^0-P) can be calculated as

$$\begin{aligned}\Delta\text{OD}_A(\epsilon_A) &\propto \text{Im}\left[\int_0^{\Delta\tau} T_A(t) e^{i\epsilon_A t}\, dt\right] \\ &\propto \text{Re}\left[1 + \frac{\Gamma_A}{2}(q_A - i)^2 \int_0^{\Delta\tau} e^{-\frac{\Gamma_A}{2}t} e^{i(\epsilon-\epsilon_A)t}\, dt\right] \\ &\propto \text{Re}\left[1 + \frac{(q_A - i)^2}{1 - i\epsilon_A}\left(1 - e^{-\frac{\Gamma_A}{2}(1-i\epsilon_A)\Delta\tau}\right)\right].\end{aligned} \tag{D6}$$

Similarly,

$$\Delta\text{OD}_B(\epsilon_B) \propto \text{Re}\left[1 + \frac{(q_B - i)^2}{1 - i\epsilon_B}\left(1 - e^{-\frac{\Gamma_B}{2}(1-i\epsilon_B)\Delta\tau}\right)\right]. \tag{D7}$$

Now, the final time-dependent double resonance spectra can be calculated as

$$\Delta\text{OD}|_{\Delta\tau} = (\Delta\text{OD}_A \times \Delta\text{OD}_B)(E)|_{\Delta\tau}. \tag{D8}$$

This can be written in the actual analytical form, which can be plotted to generate the transient double Fano spectra in terms of variable probe delay ($\Delta\tau$),

$$\begin{aligned}\Delta\text{OD}|_{\Delta\tau} \propto\ \text{Re}\Bigg\{&\left[1 + \frac{(q_A - i)^2}{1 - i\epsilon_A}\left(1 - e^{-\frac{\Gamma_A}{2}(1-i\epsilon_A)\Delta\tau}\right)\right] \\ &\times\left[1 + \frac{(q_B - i)^2}{1 - i\epsilon_B}\left(1 - e^{-\frac{\Gamma_B}{2}(1-i\epsilon_B)\Delta\tau}\right)\right]\Bigg\}.\end{aligned} \tag{D9}$$

This generates the time-domain response of the double Fano resonance and the associated time-dependent Fano parameters for both of the exciton-plasmon overlaps.

It is interesting to note that at a very large probe delay ($\Delta\tau \to \infty$), Eq. (D9) can be reduced to a steady-state Fano profile, given as

$$\Delta\text{OD}|_{\Delta\tau\to\infty} \propto \frac{(q_A + \epsilon_A)^2}{1 + \epsilon_A^2} \times \frac{(q_B + \epsilon_B)^2}{1 + \epsilon_B^2}. \tag{D10}$$

[1] B. Luk'yanchuk, N. I. Zheludev, S. A. Maier, N. J. Halas, P. Nordlander, H. Giessen, and C. T. Chong, Nat. Mater. **9**, 707 (2010).

[2] A. E. Miroshnichenko, S. Flach, and Y. S. Kivshar, Rev. Mod. Phys. **82**, 2257 (2010).

[3] M. F. Limonov, M. V. Rybin, A. N. Poddubny, and Y. S. Kivshar, Nat. Photonics **11**, 543 (2017).

[4] R. P. Madden and K. Codling, Phys. Rev. Lett. **10**, 516 (1963).

[5] U. Fano, Phys. Rev. **124**, 1866 (1961).

[6] A. Kaldun, A. Blättermann, V. Stooß, S. Donsa, H. Wei, R. Pazourek, S. Nagele, C. Ott, C. D. Lin, J. Burgdörfer, and T. Pfeifer, Science **354**, 738 (2016).

[7] V. Gruson, L. Barreau, Á. Jiménez-Galan, F. Risoud, J. Caillat, A. Maquet, B. Carré, F. Lepetit, J. F. Hergott, T. Ruchon, and L. Argenti, Science **354**, 734 (2016).

[8] C. Ott, A. Kaldun, L. Argenti, P. Raith, K. Meyer, M. Laux, Y. Zhang, A. Blättermann, S. Hagstotz,

T. Ding, and R. Heck, Nature (London) **516**, 374 (2014).

[9] C. Ott, A. Kaldun, P. Raith, K. Meyer, M. Laux, J. Evers, C. H. Keitel, C. H. Greene, and T. Pfeifer, Science **340**, 716 (2013).

[10] C. Ott, L. Aufleger, T. Ding, M. Rebholz, A. Magunia, M. Hartmann, V. Stooss, D. Wachs, P. Birk, G. D. Borisova, K. Meyer, P. Rupprecht, C. da Costa Castanheira, R. Moshammer, A. R. Attar, T. Gaumnitz, Z. H. Loh, S. Dusterer, R. Treusch, J. Ullrich, Y. Jiang, M. Meyer, P. Lambropoulos, and T. Pfeifer, Phys. Rev. Lett. **123**, 163201 (2019).

[11] J. D. Lee, J. Inoue, and M. Hase, Phys. Rev. Lett. **97**, 157405 (2006).

[12] R. A. Shah, N. F. Scherer, M. Pelton, and S. K. Gray, Phys. Rev. B **88**, 075411 (2013).

[13] W. Zhang, A. O. Govorov, and G. W. Bryant, Phys. Rev. Lett. **97**, 146804 (2006).

[14] M. Wickenhauser, J. Burgdörfer, F. Krausz, and M. Drescher, Phys. Rev. Lett. **94**, 023002 (2005).

[15] M. Hase, M. Kitajima, A. M. Constantinescu, and H. Petek, Nature (London) **426**, 51 (2003).

[16] T. Pfeifer, W. Kütt, H. Kurz, and R. Scholz, Phys. Rev. Lett. **69**, 3248 (1992).

[17] U. Siegner, M. A. Mycek, S. Glutsch, and D. S. Chemla, Phys. Rev. Lett. **74**, 470 (1995).

[18] M. V. Marquezini, P. Kner, S. Bar-Ad, J. Tignon, and D. S. Chemla, Phys. Rev. B **57**, 3745 (1998).

[19] G. Wang, A. Chernikov, M. M. Glazov, T. F. Heinz, X. Marie, T. Amand, and B. Urbaszek, Rev. Mod. Phys. **90**, 021001 (2018).

[20] R. K. Chowdhury, S. Nandy, S. Bhattacharya, M. Karmakar, S. N. Bhaktha, P. K. Datta, A. Taraphder, and S. K. Ray, 2D Mater. **6**, 015011 (2018).

[21] K. F. Mak, C. Lee, J. Hone, J. Shan, and T. F. Heinz, Phys. Rev. Lett. **105**, 136805 (2010).

[22] E. Ridolfi, C. H. Lewenkopf, and V. M. Pereira, Phys. Rev. B **97**, 205409 (2018).

[23] X. Gan, Y. Gao, K. Fai Mak, X. Yao, R. J. Shiue, A. Van Der Zande, M. E. Trusheim, F. Hatami, T. F. Heinz, J. Hone, and D. Englund, Appl. Phys. Lett. **103**, 181119 (2013).

[24] X. Liu, T. Galfsky, Z. Sun, F. Xia, E. C. Lin, Y. H. Lee, S. Kéna-Cohen, and V. M. Menon, Nat. Photonics **9**, 30 (2015).

[25] B. Lee, J. Park, G. H. Han, H. S. Ee, C. H. Naylor, W. Liu, A. C. Johnson, and R. Agarwal, Nano Lett. **15**, 3646 (2015).

[26] M. Wang, A. Krasnok, T. Zhang, L. Scarabelli, H. Liu, Z. Wu, L. M. Liz-Marzán, M. Terrones, A. Alù, and Y. Zheng, Adv. Mater. **30**, 1705779 (2018).

[27] M. Wang, Z. Wu, A. Krasnok, T. Zhang, M. Liu, H. Liu, L. Scarabelli, J. Fang, L. M. Liz-Marzán, M. Terrones, A. Alù, and Y. Zheng, Small **15**, 1900982 (2019).

[28] Z. Chi, H. Chen, Z. Chen, Q. Zhao, H. Chen, and Y. X. Weng, ACS Nano **12**, 8961 (2018).

[29] See Supplemental Material at http://link.aps.org/supplemental/10.1103/PhysRevB.101.245442 for characterization of pristine MoS_2 and additional double Fano results for the Au-MoS_2 hybrid.

[30] W. Wang, P. Vasa, R. Pomraenke, R. Vogelgesang, A. D. Sio, E. Sommer, M. Maiuri, C. Manzoni, G. Cerullo, and C. Lienau, ACS Nano **8**, 1056 (2014).

[31] L. Argenti, R. Pazourek, J. Feist, S. Nagele, M. Liertzer, E. Persson, J. Burgdörfer, and E. Lindroth, Phys. Rev. A **87**, 053405 (2013).

[32] N. Liu, T. Weiss, M. Mesch, L. Langguth, U. Eigenthaler, M. Hirscher, C. Sonnichsen, and H. Giessen, Nano Lett. **10**, 1103 (2010).

[33] I. S. Grudinin, H. Lee, O. Painter, and K. J. Vahala, Phys. Rev. Lett. **104**, 083901 (2010).

[34] S. Zhang, D. A. Genov, Y. Wang, M. Liu, and X. Zhang, Phys. Rev. Lett. **101**, 047401 (2008).

[35] W. C. Chu and C. D. Lin, Phys. Rev. A **82**, 053415 (2010).